

# Northumbria Research Link

Citation: Bainbridge, Rupert, Lim, Michael, Dunning, Stuart, Winter, Mike G., Diaz-Moreno, Alejandro, Martin, James, Torun, Hamdi, Sparkes, Bradley, Khan, Muhammad Waqas and Jin, Nanlin (2022) Detection and forecasting of shallow landslides: lessons from a natural laboratory. *Geomatics, Natural Hazards and Risk*, 13 (1). pp. 686-704. ISSN 1947-5705

Published by: Taylor & Francis

URL: <https://doi.org/10.1080/19475705.2022.2041108>  
<<https://doi.org/10.1080/19475705.2022.2041108>>

This version was downloaded from Northumbria Research Link:  
<http://nrl.northumbria.ac.uk/id/eprint/48406/>

Northumbria University has developed Northumbria Research Link (NRL) to enable users to access the University's research output. Copyright © and moral rights for items on NRL are retained by the individual author(s) and/or other copyright owners. Single copies of full items can be reproduced, displayed or performed, and given to third parties in any format or medium for personal research or study, educational, or not-for-profit purposes without prior permission or charge, provided the authors, title and full bibliographic details are given, as well as a hyperlink and/or URL to the original metadata page. The content must not be changed in any way. Full items must not be sold commercially in any format or medium without formal permission of the copyright holder. The full policy is available online: <http://nrl.northumbria.ac.uk/policies.html>

This document may differ from the final, published version of the research and has been made available online in accordance with publisher policies. To read and/or cite from the published version of the research, please visit the publisher's website (a subscription may be required.)

1 **Detection and forecasting of shallow landslides: lessons from a natural laboratory**

2

3 **Rupert Bainbridge<sup>1</sup>, Michael Lim<sup>2</sup>, Stuart Dunning<sup>1</sup>, Mike G. Winter<sup>3</sup>, Alejandro Diaz-**  
4 **Moreno<sup>1,4</sup>, James Martin<sup>2</sup>, Hamdi Torun<sup>2</sup>, Bradley Sparkes<sup>5</sup>, Muhammad Khan<sup>2</sup>,**  
5 **Nanlin Jin<sup>2</sup>**

6 <sup>1</sup> Department of Geography, Newcastle University, Newcastle, NE1 7RU, UK.

7 <sup>2</sup> Faculty of Engineering and Environment, Northumbria University, Newcastle, NE1 8ST,  
8 UK.

9 <sup>3</sup> Winter Associates, Kirknewton, Midlothian, EH27 8AF, UK.

10 <sup>4</sup> Reynolds International Ltd, Broncoed Business Park, Wrexham Rd, Mold, CH7 1HP

11 <sup>5</sup> Bridgeway Consulting, Bridgeway House, Riverside Way, Nottingham NG2 1DP, UK.

12

13 Corresponding author: Rupert Bainbridge ([rupert.bainbridge@newcastle.ac.uk](mailto:rupert.bainbridge@newcastle.ac.uk))

14

15 **Key words: Debris flow, detection, forecasting, thresholds, monitoring**

## 16 **Abstract**

17         Shallow-rapid landslides are a significant hillslope erosion mechanism and limited  
18 understanding of their initiation and development results in persistent risk to infrastructure.  
19 Here, we analyse the slope above the strategic A83 Rest and be Thankful road in the west of  
20 Scotland. An inventory of 70 landslides (2003-2020) shows three types of shallow landslide,  
21 debris flows, creep deformation and debris falls. Debris flows dominate and account for 5,350  
22 m<sup>3</sup> (98 %) of shallow-landslide source volume across the site. We use novel time-lapse vector  
23 tracking to detect and quantify slope instabilities, whilst seismometers demonstrate the potential  
24 for live detection and location of debris flows. Using on-slope rainfall data, we show that  
25 shallow-landslides are typically triggered by abrupt changes in the rainfall trend, characterised  
26 by high-intensity, long duration rainstorms, sometimes part of larger seasonal rainfall changes.  
27 We derive empirical antecedent precipitation (>62mm) and intensity-duration (>10 hours)  
28 thresholds over which shallow-landslides occur. Analysis shows the new thresholds are more  
29 effective at raising hazard alerts than the current management plan.

30         The low-cost sensors provide vital notification of increasing hazard, the initiation of  
31 movement, and final failure. This approach offers considerable advances to support operational  
32 decision-making for infrastructure threatened by complex slope hazards.

## 33 **1. Introduction**

34         Shallow landslides occur where material fails in the upper layers of a soil profile, usually  
35 up to ~2m depth. These landslides usually have little precursory warning and may fail rapidly  
36 (e.g. debris flow; [Persichillo et al., 2016](#)) or slowly (e.g. creep deformation; [Hung et al., 2014](#)).  
37 Their unpredictability means they pose a significant global hazard, particularly when  
38 favourable material and fluidisation conditions transform them into debris flows (e.g.  
39 [Zimmerman et al., 2020](#)). Debris flows are extremely rapid (>5 m/s), saturated debris-rich

40 landslides that exist along the broad spectrum of flow-like landslides (Hungr et al., 2014).  
41 Debris flow runout potential and their capacity to entrain large quantities of water and sediment  
42 make them a significant risk where linear infrastructure traverses affected slopes (Geertsema et  
43 al., 2009; Meyer et al., 2015). Debris flows can be broadly grouped into channelized debris  
44 flows (CDFs) that are constrained for their flow path and hillslope (or open slope) debris flows  
45 (HDFs) that occur on non-incised slopes (Chen et al., 2009). CDFs and HDFs can transition  
46 into one another where HDFs meet gullies or CDFs breach channels and flow over slopes; it is  
47 this hillslope-gully coupling that can control the hazard potential (Milne et al., 2009). CDFs  
48 often occur in torrent systems, such as the Illgraben, Switzerland (Badoux et al., 2009), where  
49 the repeated flow path removes some of the spatial risk uncertainty and allows focussed  
50 monitoring of a single outflow channel.

51         However, at some sites historic evidence shows debris flows may occur from anywhere  
52 across wide areas with suitable topography and materials. This leads to both spatial and  
53 temporal uncertainty on triggering location and runout. At such sites, where the risk is high, a  
54 combination of active mitigation (physically controlling site aspects using barrier, net, pit, or  
55 deflection engineering infrastructure) and passive mitigation (reducing impacts via land-use  
56 planning, closures, and warning systems) methods can be used (Huebl and Fiebiger, 2005;  
57 Vagnon, 2020) but can be costly given the wide area of potential source and runout zones. In  
58 Scotland, debris flows have repeatedly damaged roads and rail lines resulting in economic and  
59 social costs (Winter et al., 2019a), with many valleys showing historic (and prehistoric)  
60 evidence of multiple debris flow deposits slope wide (Innes, 1983; Luckman, 1992; Curry,  
61 2000). Contemporary infrastructure damaging debris flows have often been linked to high-  
62 intensity rainfall (Winter et al., 2019b). Climate forecasts suggest that in the future Scotland  
63 may receive more high intensity rainfall events in the winter and lower-frequency but higher-  
64 intensity rainfall during summer months (Finlayson, 2020; UKCP, 2018, Jones et al., 2013).

65 Such changes in antecedent conditions and rainfall patterns may perturb hillslope sediment  
66 cascades (Bennett et al., 2014), releasing sediment from storage that is considered dormant,  
67 increasing the shallow-rapid landslide hazard in mountainous areas (Winter and Shearer, 2017).

68 Monitoring strategies for determining the level of landslide hazard posed by rainfall, in  
69 a given area or slope, vary from global to hyper-local in scale. Global determination of landslide  
70 hazard requires the combination of variables such as slope, lithology, soil wetness, antecedent  
71 rainfall, and rainfall (Stanley et al., 2021). Whilst useful for global and regional indications of  
72 landslide hazard, these global models do not allow detailed analysis of areas smaller than the  
73 resolution of the data. Input data are at coarse resolution which do not always accurately  
74 represent the real-world spatial variability (Ozturk et al., 2021), making predictions noisy or  
75 imprecise. Where a higher confidence in the level of landslide hazard is required for decision  
76 making at linear infrastructure for example, hyper-local monitoring can be deployed. Hyper-  
77 local monitoring collects the detail required to make site specific thresholds for landslide  
78 initiation and makes significant improvements over global landslide susceptibility models  
79 (Ozturk et al., 2021).

80 Here we demonstrate a novel combination of near-real-time, multi-disciplinary,  
81 monitoring techniques that allow remote detection and quantification of slope changes and  
82 supplement the regional Landslide Management Plan (LMP). The objective of these techniques  
83 is to improve our understanding of shallow-rapid landslide trigger mechanisms that threaten  
84 road users and infrastructure, and thus enhance alert capabilities for road asset managers at sites  
85 that are debris flow prone to shallow-landslide / debris flow transitions. These new, relatively  
86 low-cost, monitoring techniques and analyses are essential in helping to better manage the  
87 present and future increased risk of debris flows.

## 88        2. Study area

89            The A83 Rest and be Thankful (RabT), a key road into and out of west Scotland (Fig.  
90 1a), bisects the south-western slope of Beinn Luibhean upslope from Glen Croe. This ~1.5 km  
91 section of road has the highest infrastructure damaging landslide frequency on the Scottish road  
92 network (McMillan and Holt, 2019). The average slope of the RabT is ~32° with a relief of  
93 ~580 m. The bedrock is Schist, with overlying glacial till up to 3 m thick, interspersed with  
94 gullies, landslide source scars, levees and lower slope debris cones (Sparkes et al., 2017,  
95 Finlayson, 2020, BGS, 2020). The surficial till deposits extend beyond the RabT site and cover  
96 much of the lower and mid-slopes of the surrounding hills in the Trossachs mountain range  
97 (BGS, 2020) where the A83 and other strategic roads route to the west and north of Scotland.

98            Average annual rainfall from 2013-2019 at the Scottish Environmental Protection  
99 Agency (SEPA) Rest and Be Thankful rainfall gauge, located approximately 750 m away from  
100 the RabT slope, is 3118 mm per year, with on average most rainfall occurring in October to  
101 February (Fig 1b). However, August also appears to be generally as wet as winter months and  
102 there is considerable variation in monthly rainfall between different years (Fig. 1b). The RabT  
103 is a good proxy for many sediment laden upland / mountainous systems subject to moderate to  
104 high rainfall that are susceptible to a range of slope instabilities and threaten infrastructure.

105            On average 4,000 vehicles cross the RabT per day (Winter et al., 2019a). Closures divert  
106 traffic a maximum ~88 km, if the A83 and Old Military Road (OMR; Fig. 1c), a one-way  
107 convoy diversion downslope of the A83, are closed, casting a vulnerability shadow over 4,300  
108 km<sup>2</sup> (Fig. 1a; Winter et al., 2019a). A full road closure costs ~£90k per day (2012 prices; Winter  
109 et al., 2019a) and £13.3 M has been spent on active protection of the A83, using catch-nets,  
110 catch-pits and culvert upgrades (Fig. 1c and d). This cost also includes improving the OMR to  
111 handle larger vehicles and higher traffic volumes (Scottish Parliament, 2020). However, some  
112 debris flows still exceed mitigation measures and impact the A83 and OMR. From the August

113 2020 to January 2021 the A83 was closed for ~120 days, due to a series of large debris flows  
114 in August and September 2020 (Fig. 1c). The OMR convoy diversion was in place for much of  
115 the closure time, but additional investment was made to build a 175 m long, 6.6 m tall barrier,  
116 completed in January 2021 which protects part of the OMR from debris flows (Fig. 1e). The  
117 barrier was installed as a response to the August-September 2020 debris flows and a period of  
118 persistent slope creep above the A83 following those events.

119 The Scottish Road Network Landslide Study examined the full road network landslide  
120 risk and mitigation options (Winter et al., 2005). As a result, semi-quantitative and quantitative  
121 risk assessments justified additional passive mitigation measures at the RabT (Winter et al.,  
122 2009; Winter and Wong, 2020); as part of the LMP daylight patrols are dispatched and warning  
123 lights activated on the RabT approach if forecast rainfall is  $\geq 25$  mm in a 24-hour period or  
124  $\geq 4$  mm in a 3-hour period (Winter et al., 2020), indicating a raised risk of shallow landslides  
125 and therefore debris flows.

### 126 **3. Datasets and Methodology**

#### 127 **3.1 Landslide inventories**

128 We have collated a new RabT shallow landslide inventory (available from the  
129 Newcastle University Data Repository - <https://figshare.com/s/058074e7a14320a994ce>) from  
130 road reports (2003-2015), quarterly and event responsive terrestrial laser scans (TLS; 2015-  
131 2020), and time-lapse imagery (2017-2020). Post-2015 it is unlikely events are missing as TLS  
132 (0.1 m resolution) and time-lapse imagery data were used (Sparkes et al., 2017; Khan et al.,  
133 2021, and this study). Pre-2015, debris flows that reached the A83 are recorded, but other  
134 shallow landslides that did not reach the road may not be. The quarterly and event response  
135 TLS point cloud data were used to quantify the volume of landslide source areas using the  
136 Multiscale Model to Model Cloud Comparison plugin (M3C2; Lague et al., 2013) in Cloud

137 Compare (Version 2.11.3 Anoaia; <http://www.cloudcompare.org/>), which computes distances  
138 between two referenced point clouds to show 3D change. The resulting change data were  
139 filtered to extract point-to-point losses and gains due to movement of material on the RabT  
140 slope. Longitudinal profiles of CDF and HDF source areas have been extracted from TLS point  
141 cloud derived digital elevation models (DEMs) of the RabT slope in QT Modeler (Version  
142 8070, Applied Imagery).

### 143 **3.2 Rainfall thresholds for landslide alerts**

144 Rainfall on seasonal, daily and 15-minute timescales are used here as indicators of  
145 increased shallow landslide hazard at the RabT. The 2013-2019 seasonal rainfall trend was  
146 examined for the Scottish Environment Protection Agency (SEPA) RabT rain gauge data  
147 (SEPA, 2020) using the Bayesian Estimator of Abrupt change, Seasonality and Trend (BEAST)  
148 analysis package (Zhao et al., 2019). BEAST uses ensemble modelling, where multiple  
149 competing models analyse data, and Bayesian statistics derive a model average with associated  
150 probabilities that detect if seasonal and trend changes are ‘true’. BEAST identifies seasonal  
151 change points (SCPs) when rainfall has large inter-annual variations, i.e. the seasonal  
152 component of the rainfall time-series changes between the same time in different years. Trend  
153 change points (TCPs) are identified when the rainfall time-series trend changes abruptly. For  
154 seasonal and trend components, not all variations will lead to SCPs and TCPs being assigned,  
155 only those that have a high probability of being a genuine and significant difference, based on  
156 the agreement between competing models.

157 September to December 2018 was a particularly active landslide period at the RabT and  
158 the start of high-temporal and high-spatial resolution datasets at the site, enabling the  
159 association of shallow landslide occurrence to rainfall conditions. Therefore, this period is used  
160 to look in detail at rainfall conditions at and prior to shallow landslide occurrence.

161 We calculated the Antecedent Precipitation Index (API; Fedora and Beschta, 1989), a  
162 proxy for ground saturation (Segoni et al., 2018), for daily rainfall totals using Equation 1, as  
163 an indicator of raised shallow landslide hazard.

$$164 \quad API_i = k(API_{i-1}) + P_i \quad (1)$$

165 Where  $API_i$  is the API at time  $i$ ,  $P_i$  is the daily rainfall total at  $i$  and  $k$  is a constant decay  
166 function defined by the user ( $k=0.8$ ). The  $k$  value is a conservative estimate based on other  
167 works (Heggen, 2001; Viessman and Lewis 1996, Fedora and Beschta, 1989) as no stream  
168 gauge data is available for Glen Croe, so storm hydrograph regression analysis to derive a local  
169  $k$  estimate was not possible. Rainfall has been measured with an on-slope Davis Vantage Pro 2  
170 gauge (364 m a.s.l) since April 2018, better reflecting on-slope conditions than the off-slope  
171 SEPA gauge that 0.85 km away and 87 m lower in the valley.

172 Using 15-minute rainfall intensity data from the on-slope Davis Vantage Pro 2 gauge,  
173 we developed an intensity-duration (I-D) threshold over which shallow landslides have  
174 occurred in the past. Duration and mean rain intensity for all storms in the study period were  
175 plotted (Brunetti et al., 2010; Guzzetti et al., 2008), with a six-hour inter-event period. An I-D  
176 threshold above which landslides occur was visually derived from the results (Guzzetti et al.,  
177 2008). Mean rain intensity over an entire storm was used, as opposed to mean rain intensity up  
178 to the point of the landslide, as not all landslide timings were known due to occlusion of the  
179 time lapse camera from the slope from clouds and night-time.

### 180 **3.3 Landslide initiation, tracking and detection**

181 Remote monitoring to detect slope changes can be useful for assessing slope conditions  
182 and managing infrastructure, without needing a constant personnel presence on-site. Visual  
183 analysis of imagery is useful, however an ability to analyse images pixel-by-pixel, detect  
184 changes, and quantify rates of movement provides more data to asset managers. With this ability  
185 large areas can be analysed for precursory movement before landslides occur as well as tracking

186 and detecting movement during slope failures. Here, we process time-lapse imagery in a particle  
187 image velocimetry tool (PIVLab; Thielicke and Stamhuis, 2014; Thielicke, 2020) to detect  
188 creeping deformation on the RabT during mid- to late-September 2018, before a series of road-  
189 closing debris flows in October 2018. This time-period is used here as a good example of what  
190 this technology and these data can achieve prior to a series of large slope failures. This PIV tool  
191 has since been enhanced by Khan et al., (2021) for automatic image stabilisation, processing,  
192 and filtering. Displacement vectors and velocity were established between consecutive slope-  
193 wide images at 16x16 pixel resolution ( $\sim 2.7 \text{ m}^2$ ). Sequential deformation was derived for a  
194 point tracked through the photo sequence and inverse velocity (I-V), an analytical approach  
195 used to predict failure in brittle materials (Carlà et al., 2017), was used as an indicative metric  
196 for till failure prediction. Despite the non-brittle materials involved, some shallow landslides at  
197 the RabT appear to move as rafts of intact material over a discrete, progressively forming shear  
198 surface, and, as such have more in common with brittle failure than ductile deformation.  
199 Imminent failure is predicted when I-V values reach zero (infinite velocity), in theory, and,  
200 occasionally in practice this time can be derived from monitoring data (Fan et al., 2019; Xu et  
201 al., 2020). Intervals between usable daylight images was not uniform due to cloud, rain, and  
202 night-time obscuration, so velocity data from PIVLab were interpolated to 12h intervals, with  
203 a moving average smoothing of 24h. I-V was calculated for smoothed data using  $I/(Vw)$  (e.g.  
204 Manconi and Giordan, 2016), where  $V$  is velocity over the defined time window ( $w$ ).

205 We used seismic monitoring to detect the precise timing of the onset of a shallow  
206 landslide that transitioned to a debris flow. Industry standard seismometers are used for the  
207 detection of debris flows in catchment scale torrent systems (Walter et al., 2017) and the slope  
208 failure source areas that cause them (Burtin et al., 2016). Here we deploy a low-cost Raspberry  
209 Shake 3D seismometer (Raspberry Shake, 2020; Manconi et al., 2018) for directional detection  
210 of debris flows on a steep hillslope with uncertain flow initiation and routing, and short flow

211 paths. The seismogram trace shows characteristic debris flow signals (Burtin et al., 2016),  
212 generated through clast-clast and flow-substrate interactions, above the long-term average.  
213 Conventional seismics uses cross-correlation between stations to geolocate the event generating  
214 the seismic signal (Burtin et al., 2016). Here we use hodograms (plotting signal direction  
215 through time; Borella et al., 2019) to confirm the direction of debris flow signals to the  
216 seismometer as we only had a single station deployed on the site.

## 217 **4. Results**

218 Effective road asset management requires information on raised threats of landslide  
219 activity, significant slope changes, precursory movement and, finally, post-failure adjustment  
220 during remedial works. These data all need the context of long-term activity. This enables  
221 stakeholders to be on stand-by, pre-position resources, or proactively manage risk with targeted  
222 interventions. Here we show how the methodologies are applied to achieve alerts of high  
223 activity periods within long-term records, to quantify threshold preconditions to failure, and to  
224 create ‘event happened’ warnings that have been integrated into the management of the RabT.

### 225 **4.1 Long-term landslide activity**

226 From 2003 to 2020 there were 70 shallow landslides which presented as three different  
227 landslide types: 49 were debris flows (21 HDFs, 25 CDFs, three of unknown type); 12 slope  
228 creep events, defined as a relatively slow gravitational deformation of material; and 9 debris  
229 falls (Hungri et al., 2014), which in the case of the RabT are small  $\sim 1 \text{ m}^3$  failures of surficial  
230 material, often from the top of bedrock outcrops, which do not propagate downslope (Fig. 2).  
231 Seventeen debris flows closed the A83, on average once a year since 2003 though this masks  
232 the often clustered nature of events in time; eight reached the OMR which requires a full  
233 diversion.

234           63 of the landslides have known source locations (Fig. 3), 46% (n=29) are in till, 35%  
235 (n=22) in debris cones and 19% (n=12) in regolith; 53 have volumetric information derived  
236 from TLS (2015-2019) or estimates from reports (2007-2015). Thirty-six are debris flows,  
237 seven debris falls and ten creep deformations. Combining the debris flows and debris falls, 18%  
238 of the landslide source volume originates from the debris cones (22% of the slope by area);  
239 whilst till (61% of the slope by area) and regolith (18% of the slope by area) account for 67%  
240 and 15% of the landslide source volume respectively (Table 1). Creep landslide volumes were  
241 excluded from the above volumetric analysis, as it is not possible to accurately measure the  
242 volume of the entire moving mass from TLS data, given that much of the failed material has  
243 not been evacuated from the source area. For creep landslides it is only possible to calculate the  
244 surface volume loss. Creep landslides were found in the debris cones (n=7) and till (n=3). Most  
245 of the surface volume loss from creep deformation occurred in the debris cones (5,673 m<sup>3</sup>) and  
246 very little within the till (26 m<sup>3</sup>) despite its larger coverage over the slope (Fig. 3).

247           Volumetric contributions from different materials reflect distinct failure processes and  
248 physical controls such as depth to bedrock. Failures originating from debris cone source areas  
249 are generally long (15-50 m) and have the deepest recorded failures; there is a more varied  
250 original surface-to-failure plane depth profile from debris-cone sources (Fig. 4; Table 2). Till-  
251 based failure planes vary between 5 m and 35 m in length with a shallower depth profile  
252 (average 1.2 m); whilst regolith failures are between 5 m to 25 m with a shallow average depth  
253 profile of 0.77 m (Fig. 4). The average surface slope of the RabT is ~32° and average failure  
254 plane slopes for all material types range between 30° and 31°. Extrapolation of gully pathways  
255 from a TLS derived DEM, shows a strong coupling of source areas with stream flow paths  
256 (streams in Fig. 3).

257 **4.2 The likelihood of failure: Rainfall thresholds**

258 Rainfall on seasonal, daily, and 15-minute timescales has been used to indicate raised  
259 landslide hazard. BEAST identified six rainfall seasonal change points (SCP) in winter periods  
260 from 2013 to 2020 (Fig. 5a). SCP4 coincides with Storms Desmond and Frank which caused  
261 debris flows at the RabT. SCP6 in mid-2020 shortly precedes the large August-September  
262 debris flows that shut the A83. No SCPs are seen from 2016 to late-2019, but debris flows do  
263 still occur. Instead, many debris flows are coincident with abrupt rainfall trend change points  
264 (TCPs) as well as their subsequent falling trends, and long period high trends (Fig. 5b). TCPs  
265 1, 2, 3, 5, 6 and 9 are all associated with debris flow occurrence.

266 TCP6 starts the 2018 landslide period, a particularly active year with 19 of the 63  
267 shallow landslides (Fig. 2). Here we use September to December 2018, a particularly active  
268 time-period at the RabT, as a case study to highlight the effectiveness of pro-active, near-real-  
269 time monitoring to alert asset managers to increased shallow landslide hazard based on rainfall  
270 thresholds, tracking slope creep, and detecting debris flow occurrence. Time-lapse imagery has  
271 allowed the timings of the 2018 landslides to be more accurately detected, allowing the  
272 identification of specific rainstorms where landslides have occurred.

273 For the late-2018 period Fig. 6 shows when LMP forecast rainfall thresholds were  
274 exceeded and warning lights were operating, along with the same thresholds plotted using on-  
275 slope, live rain data. These data are summarized in confusion matrices which describe the  
276 performance of the rainfall thresholds in detecting conditions that triggered shallow landslides;  
277 data are described as times where thresholds predict landslides will or will not happen against  
278 times where landslides did or did not occur. False alarms and missed landslides account for  
279 6.9% of the study period for warning lights and 12.2% for on-slope data (Table 3).

280 Warning lights are human operated, reducing false alarms through expert judgement.  
281 However, on-slope data would raise alert levels two times where shallow landslides

282 (particularly debris flows) occurred, that are not fully covered by the warning lights (Fig. 6 i  
283 and ii). To improve on the current LMP rainfall thresholds for predicting hazardous shallow  
284 landslide conditions on the RabT, shown in Figure 6 and Table 3, we now look at the intensity  
285 and duration of rainstorms which generated landslides, and antecedent precipitation.

286 Landslide producing storms in 2018 were medium (>10h) to long duration (max. 72h;  
287 Fig. 7); however, for two storms it was not possible to determine in which the landslide  
288 happened. Mean rain intensity for landslide initiation ranges from 2.95 mm/hr to 8.15 mm/hr.  
289 Landslides occur above the threshold described by Equation 2.

$$290 \quad I = 4.75D^{-0.18} \quad (2)$$

291 Where  $I$  is mean rain intensity and  $D$  is duration. All confirmed landslide storms were >10h  
292 duration, so it is unclear if the threshold applies to storms of <10h duration. The threshold has  
293 been extrapolated for storms under 10h duration but dashed on Figure 7 to show its uncertainty.  
294 The I-D threshold gives a false alarm for 5.7% of the study period (Table 4).

295 All landslides (n=18) occur over an API threshold of 37 mm, with three false alarms  
296 and long periods of alert with no landslides (Fig. 8). A 62 mm API threshold covers 90% of  
297 landslides (n=16), reduces false alarms to 0.8% of the study period (Table 4), but misses two  
298 mid-December events. A combination of I-D and API thresholds maximizes landslide detection  
299 and minimizes false alarms (Table 4). All landslide inducing storms exceed the I-D threshold  
300 with five false alarms (Fig. 8 i to v) which API thresholds reduce to two (Fig. 8 iv, v).

### 301 **4.3 Early warning of slow creeping failures**

302 We monitored the creep of Failure 2 (Fig. 6) via time-lapse image vector tracking from  
303 initiation (19 September 2018) to arrest (27 September 2018) using PIVLab (Thielicke and  
304 Stamhuis, 2014; Thielicke, 2020; Khan et al., 2021). Vectors of change and a velocity heat map  
305 between consecutive images are shown in Figs. 9a and 9b.

306 Creep initiation coincides with a rainstorm on the 18 September 2018 (Fig. 9c i). Half  
307 of the total cumulative deformation occurs in the first 2.5 days. Inverse velocity (I-V) rapidly  
308 decreases towards zero on the 19-20 September 2018; extrapolation of the I-V trend predicts  
309 failure on the 21 September 2018. However, I-V values increase on the 21 September,  
310 indicating reduced velocity after rainfall ceases. The deformation rate slows until arrest (Fig.  
311 9c ii) and subsequent rainfall does not affect the deformation rate and (Fig. 9c iii).  
312 Operationally, alert levels would be raised in Phase i when imminent failure seemed likely but  
313 lowered in Phase ii.

#### 314 **4.4 Detecting rapid debris flows**

315 Seismic monitoring identified a HDF (Figs. 10a and 10b) on the 09 October 2018 and  
316 located the source area. The z-axis seismogram (Fig. 10c) shows a high-amplitude signal lasting  
317 ~15s, corresponding with the failure time derived from time-lapse imagery, which is likely the  
318 HDF in motion. Short duration, lower amplitude signals follow and are likely post-landslide  
319 sediment and boulder reworking. Hodograms show very little activity at first (Fig. 10c i), but  
320 signal strength increases as the HDF signal arrives (ii) before subsiding (iii). Stacked  
321 hodograms, overlain on a DEM, point to the HDF source area as the direction of the incoming  
322 signal (Fig. 10d).

323  
324 RabT debris flow seismic signals are brief due to short, steep flow paths, with boulder  
325 and sediment reworking post-event. Another deposit on Fig. 10b, which is a thin, fine-grained  
326 drape but has a large deposit footprint, was not detected by seismic monitoring; indicating that  
327 whilst high debris content flows can be detected, hyper-concentrated flows may need larger  
328 station arrays for detection.

329        **5. Discussion**

330            Between 2003 and 2020 there were 70 shallow landslides recorded, including 49 debris  
331 flows. Landslides come from three material types on the slope: regolith, till and, debris cones,  
332 which exert a control on source area morphology and landslide volumes. Debris cone sources  
333 are generally deeper, which likely represents thicker deposits of source material to bedrock.  
334 The failure depths sourced in the upslope surface material comprising of glacial till and regolith  
335 were significantly shallower. The total volume of source areas for debris flows and debris falls  
336 across the slope is 5,404 m<sup>3</sup>, with debris cones accounting for 18% (984 m<sup>3</sup>), regolith 15% (823  
337 m<sup>3</sup>) and till the remaining 67% (3,597 m<sup>3</sup>). Each material type accounts for a proportion of  
338 source volumes similar to their areal coverage of the slope, indicating that no one material  
339 produces relatively more landslide volume than any other. However, debris cones produce  
340 fewer but larger landslides, whilst till and regolith sources produce smaller but more frequent  
341 landslides. Debris flows in till have closed the road seven times compared to four and three  
342 times for regolith and debris cones respectively. Debris flows in till could therefore be  
343 considered as the greatest risk to road closure. Similar failure plane slope angles of 30° to 31°  
344 indicate a control on landslide initiation, which may represent a critical threshold within the  
345 slope material or relate to the dip angle of the underlying bedrock – although most shallow  
346 landslides at the site are not at the bedrock-cover interface.

347            BEAST rainfall analysis shows that debris flows are primarily associated with abrupt  
348 rainfall trend changes, but that in some cases there is a larger seasonal signal associated with  
349 debris flow occurrence. In the 2018 study period, antecedent, and medium- to long-duration,  
350 high-intensity rainfall is shown to be an important factor in debris flows initiation. New local  
351 API and I-D rainfall thresholds, identify all landslide inducing storms and minimize false  
352 alarms, improve on the LMP and provide road authorities time to consider actions. 90% of  
353 RabT landslides occurred over a 62 mm API, indicating a critical antecedent rainfall threshold.

354 Rainstorm I-D >10h is key for landslide initiation with largely higher mean rain intensity than  
355 non-landslide storms. Whilst the thresholds have been calculated locally at the RabT, the  
356 surface geology and the topography of the site are replicated in and representative of the  
357 surrounding mountain range, indicating that the thresholds potentially apply more regionally  
358 although there is not currently a wider, timed inventory of failures.

359 Time-lapse vector tracking located and quantified creeping deformation in response to  
360 rainfall drivers. I-V calculations forecast imminent failure in the initiation phase, however creep  
361 slowed when rainfall ceased and arrested despite further rainfall. This method can detect slope  
362 movement and indicate times of heightened risk of failure for management authorities.

363 24-7 passive seismic detection and hodograms were used to identify a HDF. In this  
364 instance, and likely others due to short RabT flow paths, the 15 second event duration is too  
365 brief for live warnings but allows for 24/7 event detection and rapid response, outside of time-  
366 lapse image capture. Additional seismometers (now deployed) extend the range of detection  
367 and allow more traditional geo-location.

## 368 **6. Conclusions**

369 This paper presents the results of on-site monitoring at the RabT, aimed at  
370 supplementing the existing regional LMP (Winter et al., 2009). Our novel combination of  
371 sensors and processing techniques allows near-real-time monitoring and quantification of  
372 shallow-rapid landslides as demonstrated at the RabT in the west of Scotland. Results show that  
373 local sensor systems improve our understanding of triggers by allowing landslides to be  
374 attributed to specific rainstorms and therefore the conditions leading to their initiation are better  
375 quantified. Improved rainfall thresholds for periods of likely increased shallow landslide hazard  
376 have be developed for the RabT, however the techniques could be readily applied to other sites  
377 of interest. Further, we have shown that creep deformation can be detected and then tracked in  
378 near-real time, and, that rapid debris flow failures (which many or may not have shown

379 precursory movement) can be detected. Low-cost sensors can be replicated at high- and lower-  
380 risk sites where cost-benefit would normally prevent monitoring. Increased high-intensity  
381 rainfall due to climate warming is expected in Scotland (UKCP, 2018), meaning more  
382 infrastructure and assets will have increased debris flow risk. These combined low-cost  
383 monitoring techniques are an essential advancement and now operationally proven approach  
384 for addressing this future risk.

385

### 386 **Acknowledgements**

387 We thank NERC (NE/P000010/1, NE/T00567X/1, NE/T005653/1), Research England  
388 (www.Pitch-in.ac.uk ‘SlopeRIoT’), Transport Scotland and the Scottish Road Research Board  
389 (SRRB) for funding. We also thank BEAR Scotland, GeoRope, Jacobs, Forestry and Land  
390 Scotland, Glencroe Farm and John Mather for research, access, and on-site support. We declare  
391 no conflicts of interest.

### 392 **Data Availability Statement**

393 Datasets for this research are available from the Newcastle University Data Repository  
394 (<https://figshare.com/s/058074e7a14320a994ce>).

### 395 **References**

- 396 Badoux, A., Graf, C., Rhyner, J., Kuntner, R. and McArdell, B.W. (2009). A debris-flow  
397 alarm system for the Alpine Illgraben catchment: design and performance. *Natural Hazards*,  
398 *49*, 517-539, <https://doi.org/10.1007/s11069-008-9303-x>
- 399 Bennett, G.L., Molnar, P., McArdell, B.W. and Burlando, P. (2014). A probabilistic sediment  
400 cascade model of sediment transfer in the Illgraben. *Water Resources Research*, *50*, 1225-  
401 1244, <https://doi.org/10.1002/2013WR013806>
- 402 BGS (2020). Onshore GeoIndex, <https://mapapps2.bgs.ac.uk/geoindex/home.html> (accessed  
403 June 2020)

404 Borella, J., Quigley, M., Krauss, Z., Lincoln, K., Attanayake, J., Stamp, L., Lanman,  
405 H., Levine, S., Hampton, S. and Gravley, D. (2019). Geologic and geomorphic controls on  
406 rockfall hazard: how well do past rockfalls predict future distributions?. *Natural Hazards and*  
407 *Earth System Sciences*, 19, 2249–2280, <https://doi.org/10.5194/nhess-19-2249-2019>

408 Brunetti M.T., Peruccacci, S., Rossi, M., Luciani, S., Valigi, D. and Guzzetti, F. (2010).  
409 Rainfall thresholds for the possible occurrence of landslides in Italy. *Natural Hazards and*  
410 *Earth Systems Science*, 10, 447-458, <https://doi.org/10.5194/nhess-10-447-2010>

411 Burtin, A., Hovius, N., McArdell, B. W., Turowski, J. M. and Vergne, J. (2016). Seismic  
412 constraints on dynamic links between geomorphic processes and routing of sediment in a  
413 steep mountain catchment. *Earth Surface Dynamics*, 2, 21–33, [https://doi.org/10.5194/esurf-](https://doi.org/10.5194/esurf-2-21-2014)  
414 [2-21-2014](https://doi.org/10.5194/esurf-2-21-2014)

415 Carlà, T., Intrieri, E., Di Traglia, F., Nolesini, T., Gigli, G. and Casagli, N. (2017). Guidelines  
416 on the use of inverse velocity method as a tool for setting alarm thresholds and forecasting  
417 landslides and structure collapses. *Landslides*, 14, 517-534, [https://doi.org/10.1007/s10346-](https://doi.org/10.1007/s10346-016-0731-5)  
418 [016-0731-5](https://doi.org/10.1007/s10346-016-0731-5)

419 Chen, J-C., Lin, C-W. and Wang, L-C. (2009). Geomorphic Characteristics of Hillslope and  
420 Channelized Debris Flows: A Case Study in the Shitou Area of Central Taiwan. *Journal of*  
421 *Mountain Science*, 6, 266-273, <https://doi.org/10.1007/s11629-009-0250-0>

422 Curry, A.M. (2000). Holocene reworking of drift-mantled hillslopes in the Scottish  
423 Highlands. *Journal of Quaternary Science*, 15, 529–541,  
424 <https://doi.org/10.1191/095968300666146993>

425 Fan, X., Xu, Q., Liu, J., Subramanian, S.S., He, C., Zhu, X. and Zhou, L. (2019). Successful  
426 early warning and emergency response of a disastrous rockslide in Guizhou province, China.  
427 *Landslides*, 16, 2445–2457, <https://doi.org/10.1007/s10346-019-01269-6>

428 Fedora, M.A. and Beschta, R.L. (1989). Storm runoff simulation using an Antecedent  
429 Precipitation Index (API) model. *Journal of Hydrology*, 112, 121-133,  
430 [https://doi.org/10.1016/0022-1694\(89\)90184-4](https://doi.org/10.1016/0022-1694(89)90184-4)

431 Finlayson, A. (2020). Glacial conditioning and paraglacial sediment reworking in Glen Croe  
432 (the Rest and be Thankful), western Scotland. *Proceedings of the Geologists' Association*,  
433 *131(2)*, 138-154, <https://doi.org/10.1016/j.pgeola.2020.02.007>

434 Gertseema, M., Schwab, J.W., Blais-Stevens, A. and Sakals, M.E. (2009). Landslides  
435 impacting linear infrastructure in west central British Columbia. *Natural Hazards*, 48, 59-72,  
436 <https://doi.org/10.1007/s11069-008-9248-0>

437 Guzzetti, F., Peruccacci, S., Rossi, M. and Stark, C.P. (2008). The rainfall intensity–duration  
438 control of shallow landslides and debris flows: an update. *Landslides*, 5, 3-17,  
439 <https://doi.org/10.1007/s10346-007-0112-1>

440 Heggen, R.J. (2001) Normalized antecedent precipitation index. *Journal of Hydrologic*  
441 *Engineering*, 6, 377-381, [https://doi.org/10.1061/\(ASCE\)1084-0699\(2001\)6:5\(377\)](https://doi.org/10.1061/(ASCE)1084-0699(2001)6:5(377))

442 Huebl, J. and Fiebiger, G. (2005). Debris-flow mitigation measures, in Jakob, M. and Hungr,  
443 O., eds., *Debris-flow Hazards and Related Phenomena*, 445-487, Springer, Berlin Heidelberg

444 Hungr, O., Leroueil, S. and Picarelli, L. (2014). The Varnes classification of landslide types,  
445 an update. *Landslides*, 11, 167-194, <https://doi.org/10.1007/s10346-013-0436-y>

446 Innes, J.L. (1983). Lichenometric dating of debris-flow deposits in the Scottish Highlands.  
447 *Earth Surface Processes and Landforms*, 8, 579-588, <https://doi.org/10.1002/esp.3290080609>

448 Jones, M.R., Fowler, H.J., Kilsby, C.G. and Blenkinsop, S. (2013). An assessment of changes  
449 in seasonal and annual extreme rainfall in the UK between 1961 and 2009. *International*  
450 *Journal of Climatology*, 33, 1178-1194, <https://doi.org/10.1002/joc.3503>

451 Khan, M.W., Dunning, S., Bainbridge, R., Martin, J., Diaz-Moreno, A., Torun, H., Jin, N.,  
452 Woodward, J. and Lim, M. (2021). Low-Cost Automatic Slope Monitoring Using Vector  
453 Tracking Analyses on Live-Streamed Time-Lapse Imagery. *Remote Sensing*, 13(5), 893,  
454 <https://doi.org/10.3390/rs13050893>

455 Lague, D., Brodu, N. and Leroux, J. (2013). Accurate 3D comparison of complex topography  
456 with terrestrial laser scanner: Application to the Rangitikei canyon (N-Z). *ISPRS Journal of*  
457 *Photogrammetry and Remote Sensing*, 82, 10-26,  
458 <https://doi.org/10.1016/j.isprsjprs.2013.04.009>

459 Luckman, B.H. (1992). Debris Flows and Snow Avalanche Landforms in the Lairig Ghru,  
460 Cairngorm Mountains, Scotland. *Geografiska Annaler: Series A, Physical Geography*, 74:2-  
461 3, 109-121, <https://doi.org/10.1080/04353676.1992.11880355>

462 Manconi, A., Coviello, V., Galletti, M. and Seifert, R. (2018). Short Communication:  
463 Monitoring rockfalls with the Raspberry Shake. *Earth Surface Dynamics*, 6, 1219-1227,  
464 <https://doi.org/10.5194/esurf-6-1219-2018>

465 Manconi, A. and Giordan, D. (2016). Landslide failure forecast in near-real-time. *Geomatics,*  
466 *Natural Hazards and Risk*, 7:2, 639-648, <https://doi.org/10.1080/19475705.2014.942388>

467 Meyer, N., Schwanghart, W., Korup, O. and Nadim, F. (2015). Roads at risk: traffic detours  
468 from debris flows in southern Norway. *Natural Hazards and Earth System Science*, 15, 985-  
469 995, <https://doi.org/10.5194/nhess-15-985-2015>

470 McMillan, F.N. and Holt, C.A. (2018). BEAR Scotland NW trunk road maintenance: efficient  
471 management of geotechnical emergencies. *Quarterly Journal of Engineering Geology and*  
472 *Hydrogeology*, 52, 286-294, <https://doi.org/10.1144/qjegh2018-035>

473 Milne, F.D., Werritty, A., Davies, M.C.R. and Brown, M.J. (2009). A recent debris flow event  
474 and implications for hazard Management. *Quarterly Journal of Engineering Geology and*  
475 *Hydrogeology*, 42, 51–60, <https://doi.org/10.1144/1470-9236/07-073>

476 Ozturk, U., Saito, H., Matsushi, Y., Crisologo, I. and Schwanghart, W. (2021). Can global  
477 rainfall estimates (satellite and reanalysis) aid landslide hindcasting?. *Landslides*, 18, 3119-  
478 3133, <https://doi.org/10.1007/s10346-021-01689-3>

479 Persichillo, M.G., Bordoni, M., Meisina, C., Bartelletti, C., Barsanti, M., Giannecchini, R.,  
480 Avanzi, G.D., Galanti, Y., Cevasco, A., Brandolini, P. and Galve, J.P. (2017). Shallow  
481 landslides susceptibility assessment in different environments. *Geomatics, Natural Hazards*  
482 *and Risk*, 8:2, 748-771, <https://doi.org/10.1080/19475705.2016.1265011>

483 Raspberry Shake. (2020). <https://raspberrysshake.org/> (accessed June 2020)

484 Scottish Parliament. (2020). Official Report of the Public Petitions Committee, 05 March  
485 2020, <http://www.parliament.scot/parliamentarybusiness/report.aspx?r=12561> (accessed, July  
486 2020)

487 Segoni, S., Rosi, A., Lagomarsino, D., Fanti, R. and Casagli, N. (2018). Brief communication:  
488 Using averaged soil moisture estimates to improve the performances of a regional-scale  
489 landslide early warning system. *Natural Hazards and Earth System Science*, 18, 807-812,  
490 <https://doi.org/10.5194/nhess-18-807-2018>

491 SEPA. (2020). Rest and Be Thankful 15-minute rainfall record,  
492 <https://www2.sepa.org.uk/rainfall/> (accessed May 2020)

493 Sparkes, B., Dunning, S., Lim, M. and Winter, M.G. (2017). Characterisation of Recent  
494 Debris Flow Activity at the Rest and Be Thankful, Scotland, in Mikoš, M., Vilímek, V., Yin,  
495 Y. and Sassa, K., eds., *Advancing Culture of Living with Landslides, Volume 5 Landslides in*

496 *Different Environments: WLF: Workshop on World Landslide Forum Conference*  
497 *Proceedings*, 51-58, [https://doi.org/10.1007/978-3-319-53483-1\\_8](https://doi.org/10.1007/978-3-319-53483-1_8)

498 Stanley, T.A., Kirschbaum, D.B., Benz, G., Emberson, R.A., Amatya, P.M., Medwedeff, W.  
499 and Clark, M.K. (2021). Data-Driven Landslide Nowcasting at the Global Scale. *Frontiers in*  
500 *Earth Science*, 9:640043, <https://doi.org/10.3389/feart.2021.640043>

501 Thielicke, W. (2020). PIVlab - particle image velocimetry (PIV) tool.  
502 [https://www.mathworks.com/matlabcentral/fileexchange/27659-pivlab-particle-image-](https://www.mathworks.com/matlabcentral/fileexchange/27659-pivlab-particle-image-velocimetry-piv-tool)  
503 [velocimetry-piv-tool](https://www.mathworks.com/matlabcentral/fileexchange/27659-pivlab-particle-image-velocimetry-piv-tool), MATLAB Central File Exchange. (Accessed July 2020)

504 Thielicke, W. and Stamhuis, E.J. (2014). PIVlab – Towards User-friendly, Affordable and  
505 Accurate Digital Particle Image Velocimetry in MATLAB. *Journal of Open Research*  
506 *Software*, 2 (1), e30. <http://doi.org/10.5334/jors.bl>

507 UKCP. (2018). UK Climate Projections. Met Office,  
508 <https://www.metoffice.gov.uk/research/approach/collaboration/ukcp/> (accessed June 2020)

509 Vagnon, F. (2020). Design of active debris flow mitigation measures: a comprehensive  
510 analysis of existing impact models. *Landslides*, 17, 313-333, [http://doi.org/10.1007/s10346-](http://doi.org/10.1007/s10346-019-01278-5)  
511 [019-01278-5](http://doi.org/10.1007/s10346-019-01278-5)

512 Viessman, W., Jr., and Lewis, G. L. (1996). Introduction to hydrology. 4th Ed.,  
513 HarperCollins, New York.

514 Walter, F., Burtin, A., McArdell, B., Hovius, N., Weder, B., Turowski, J.M. (2017). Testing  
515 seismic amplitude source location for fast debris-flow detection at Illgraben, Switzerland.  
516 *Natural Hazards and Earth System Science*, 17, 939-955, [https://doi.org/10.5194/nhess-17-](https://doi.org/10.5194/nhess-17-939-2017)  
517 [939-2017](https://doi.org/10.5194/nhess-17-939-2017)

518 Winter M.G., Macgregor F., Shackman, L. (2009). Scottish Road Network Landslides Study:  
519 Implementation, The Scottish Executive, Edinburgh

520 Winter, M.G., Peeling, D., Palmer, D. and Peeling, J. (2019a). Economic impacts of  
521 landslides and floods on a road network. *AUC Geographica*, 54(2), 207-220,  
522 <https://doi.org/10.14712/23361980.2019.18>

523 Winter, M.G., Ognissanto, F. and Martin, L.A. (2019b). Rainfall Thresholds for Landslides  
524 Deterministic and Probabilistic Approaches. *Transport Research Laboratory Published*  
525 *Project Report PPR901*, <https://trl.co.uk/reports/rainfall-thresholds-landslides>

526 Winter, M.G., Kinnear, N. and Helman, S. (2020). A technical and perceptual evaluation of a  
527 novel landslide early warning system. *Proceedings, Institution of Civil Engineers (Transport)*,  
528 <https://doi.org/10.1680/jtran.19.00138>

529 Winter, M.G. and Wong, J.C.F. (2020). The assessment of quantitative risk to road users from  
530 debris flow. *Geoenvironmental Disasters*, 7(4), 1-19, [https://doi.org/10.1186/s40677-019-](https://doi.org/10.1186/s40677-019-0140-x)  
531 0140-x

532 Xu, Q., Peng, D., Zhang, S., Zhu, X., He, C., Qi, X., Zhao, K., Xiu, D. and Ju, N. (2020).  
533 Successful implementations of a real-time and intelligent early warning system for loess  
534 landslides on the Heifangtai terrace, China. *Engineering Geology*, 278,  
535 <https://doi.org/10.1016/j.enggeo.2020.105817>

536 Zhao, K., Wulder, M.A., Hu, T., Bright, R., Wu, Q., Qin, H., Li, Y., Toman, E., Mallick, B.,  
537 Zhang, X. and Brown, M. (2019). Detecting change-point, trend, and seasonality in satellite  
538 time series data to track abrupt changes and nonlinear dynamics: A Bayesian ensemble  
539 algorithm. *Remote Sensing of Environment*, 232, <https://doi.org/10.1016/j.rse.2019.04.034>

540 Zimmerman, F., McARDell, B.W., Rickli, C. and Scheidl, C. (2020). 2D Runout Modelling of  
541 Hillslope Debris Flows, Based on Well-Documented Events in Switzerland. *Geosciences*,  
542 10(2), <https://doi.org/10.3390/geosciences10020070>

543

544

545

546

547

548

549

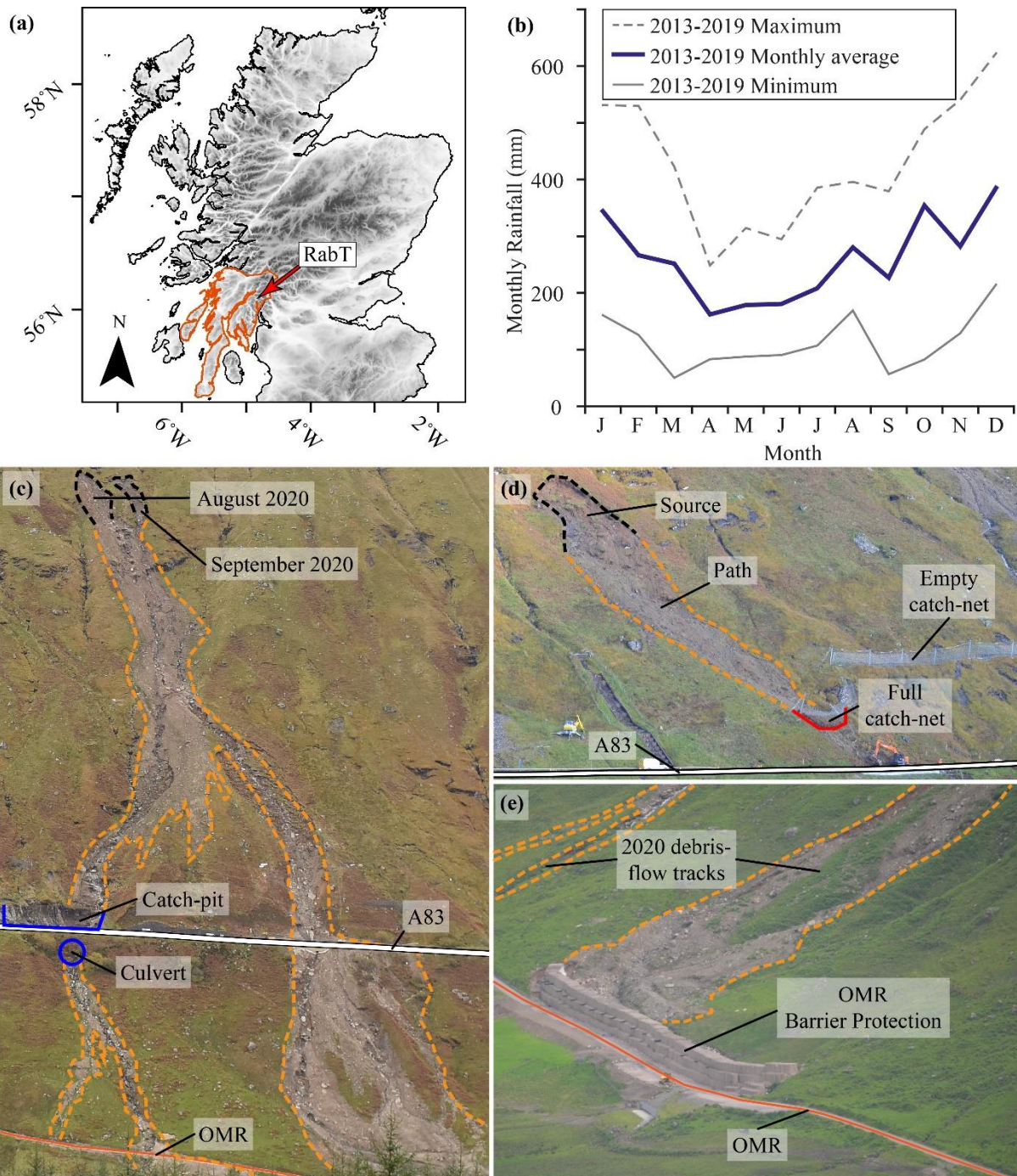
550

551

552

553

554

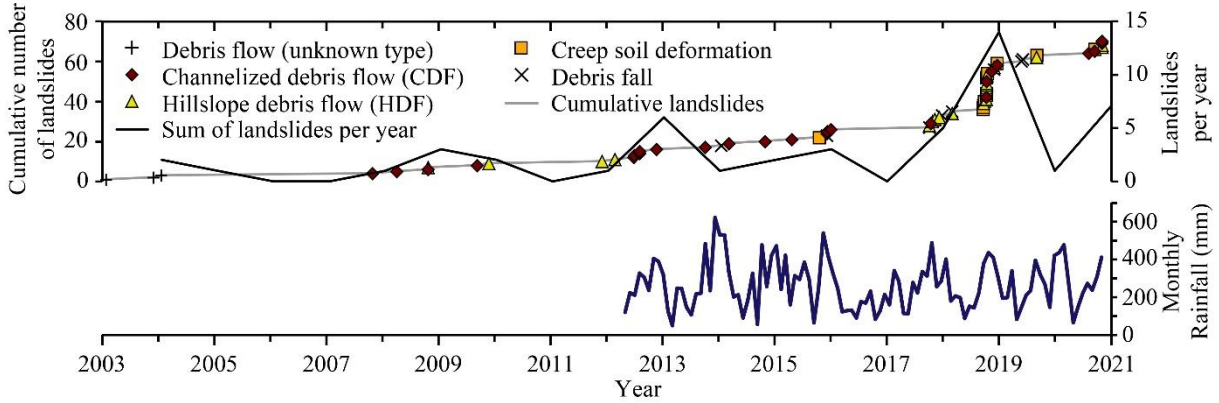


555

556 **Figure 1.** (a) Scotland digital terrain model showing the RabT location (red arrow) and the  
 557 vulnerability shadow for simultaneous A83/OMR road closures outlined in orange (modified  
 558 from Winter et al. 2019a). (b) RabT average monthly rainfall from 2013 to 2019 (SEPA RabT  
 559 gauge; SEPA, 2020). (c) Debris flows from August and September 2020 with catch-pit and  
 560 culvert mitigation. (d) October 9<sup>th</sup> 2018 debris flow which closed the A83. The catch-net has

561 caught the debris, but some has exceeded the net capacity. (e) View of the OMR debris-flow  
562 protection barrier completed in January 2021.

563

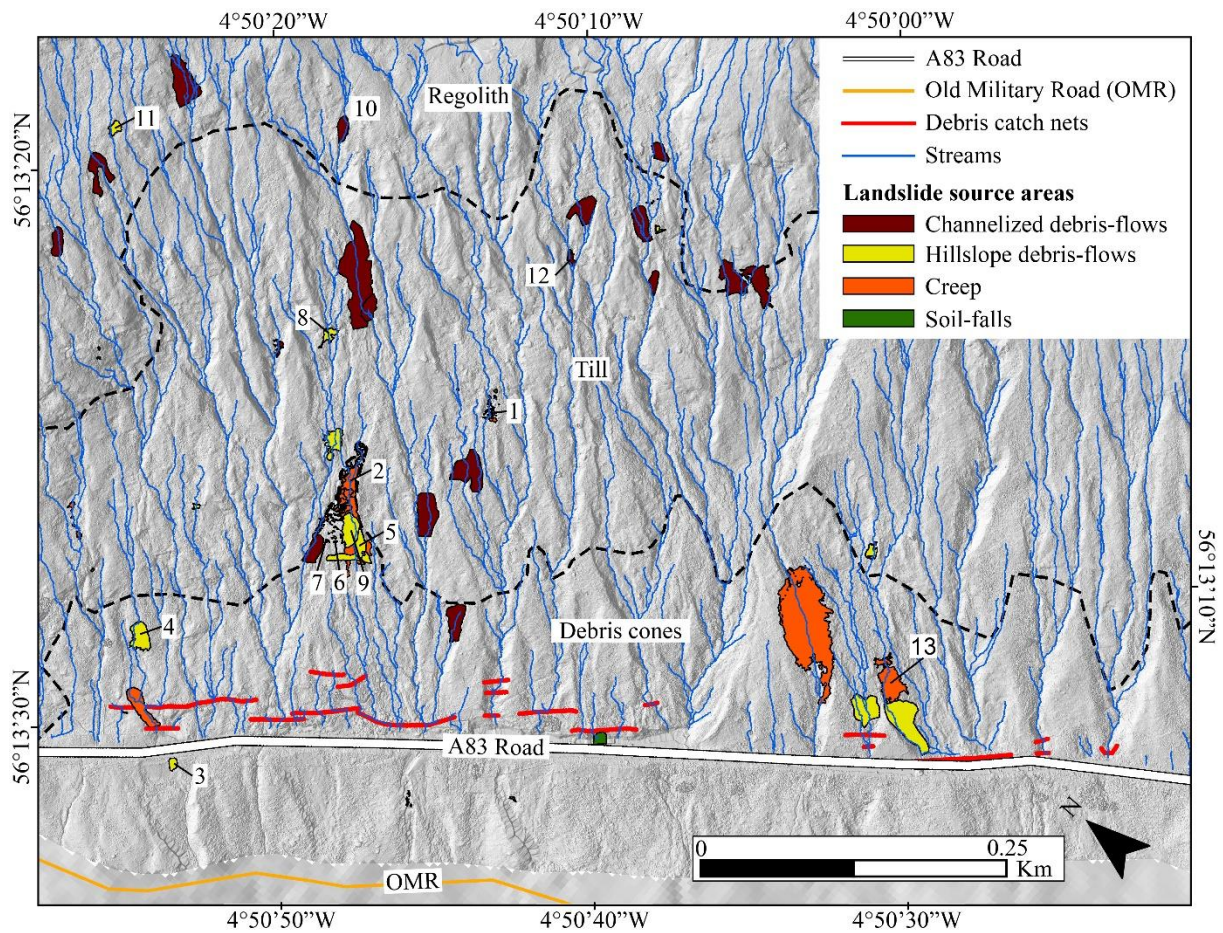


564

565 **Figure 2.** 2003 to 2020 cumulative landslide timeseries and yearly totals. Monthly rainfall is  
566 shown from the off-slope SEPA Rest and be Thankful gauge from 2012-2020 (no rainfall data  
567 was collected pre-2012).

568

569

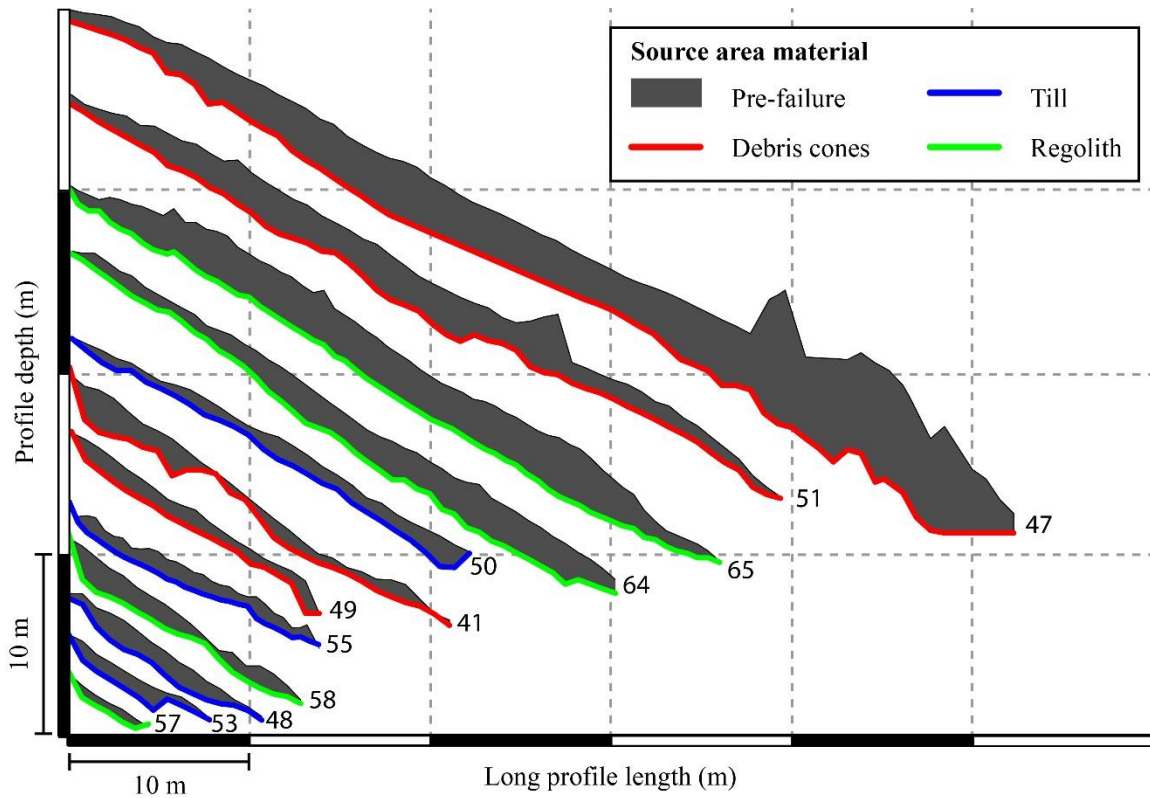


570

571 **Figure 3. RabT landslide inventory. TLS derived hillshade and 2007 to 2019 landslide**  
 572 **source areas, coloured by the resulting failure type. Surface material delineation**  
 573 **(dashed lines) modified from Finlayson, 2020. Numbers refer to Fig. 6.**

574

575

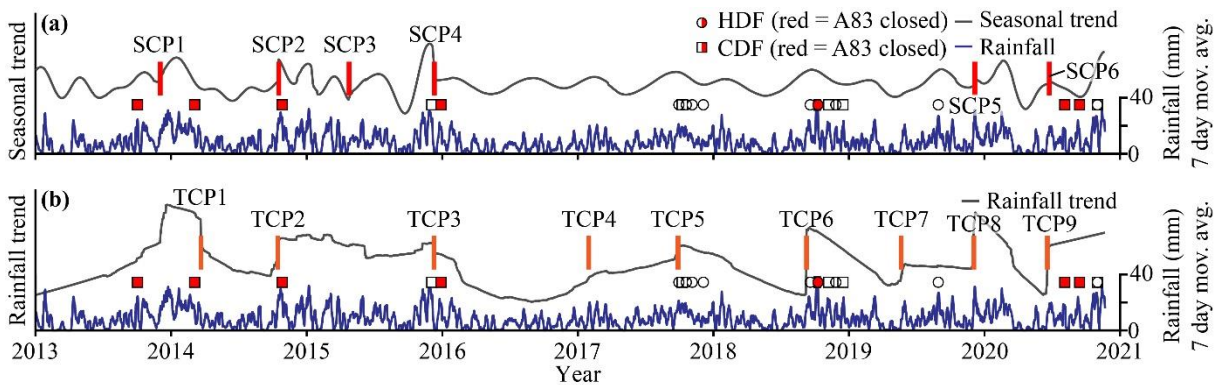


576

577 **Figure 4. Example debris flow source area long profiles (2018-2020), derived from TLS**  
 578 **point clouds, showing pre- and post-failure surface elevations. Profiles are coloured by**  
 579 **source material type. Profiles are numbered by the landslide inventory.**

580

581



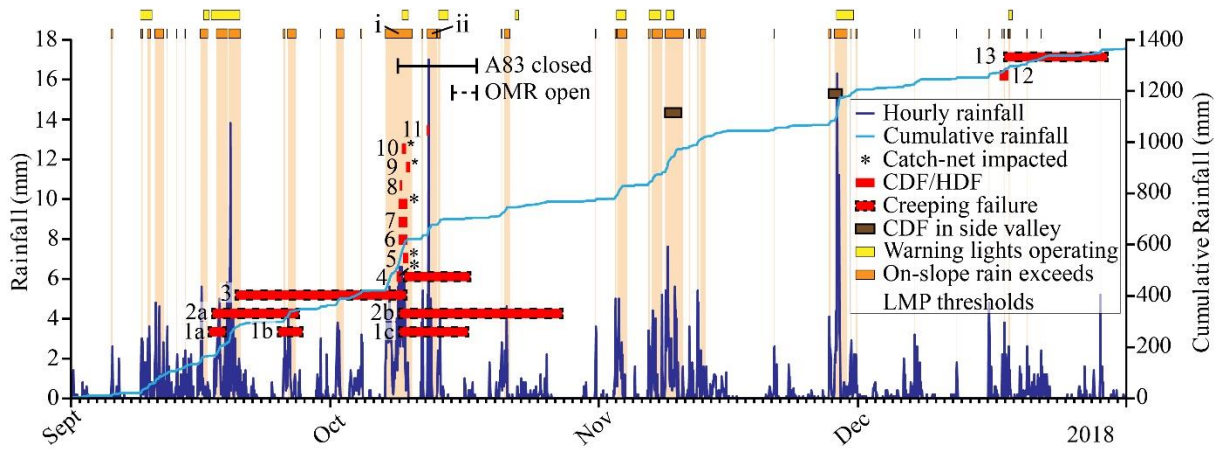
582

583 **Figure 5. (a) BEAST seasonal rainfall component. (b) BEAST rainfall trend.**

584

585

586



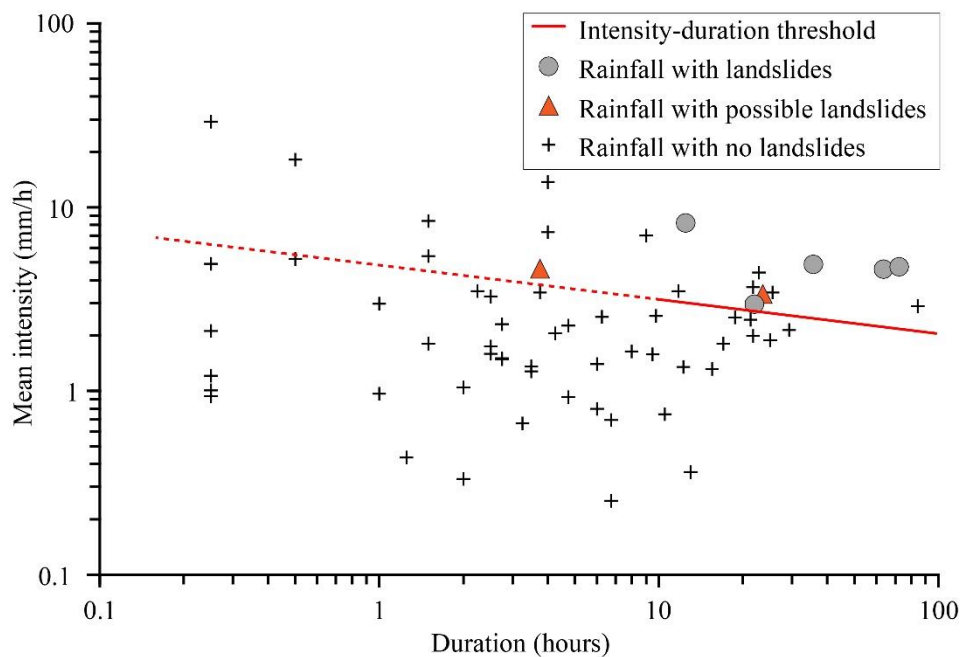
587

588 **Figure 6.** 01 September to 31 December 2018 landslides, warning light activations from the  
 589 current LMP thresholds (where forecast data is used) and activations that would have occurred  
 590 using real-time on-slope data. On-slope rainfall data is from the Newcastle University Davis  
 591 gauge.

592

593

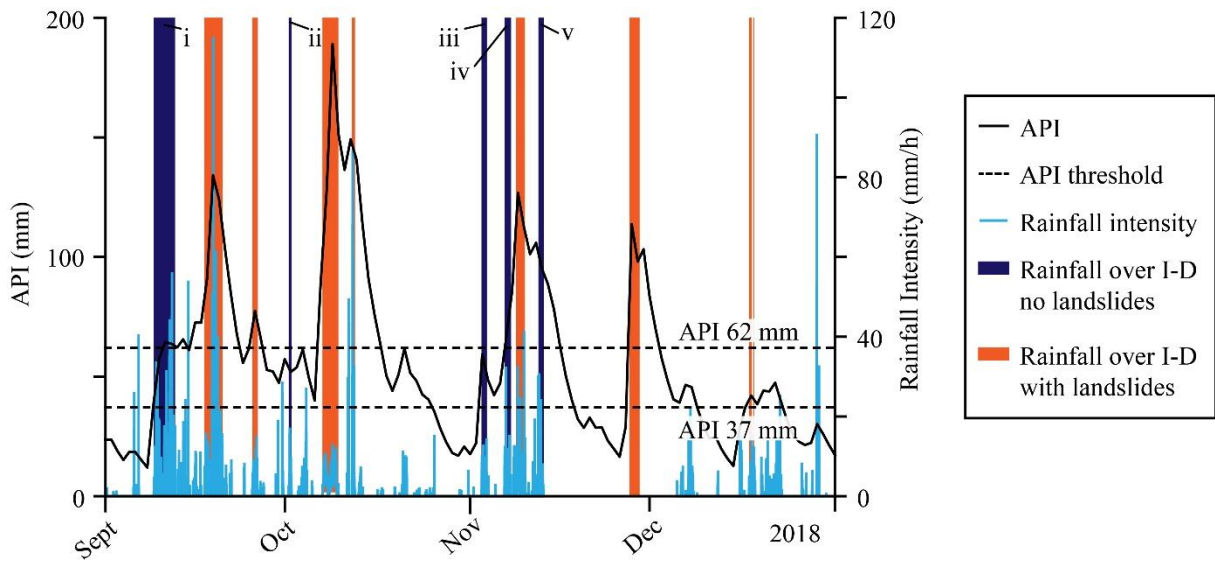
594



595

596 **Figure 7.** September to December rainstorm intensity-duration (I-D) plot. The solid red line is  
 597 the intensity-duration threshold above 10 hours duration. Below 10h duration the threshold is a  
 598 dashed red line as there was no input data for <10h landslide inducing rainstorms, this is an  
 599 extrapolation.

600



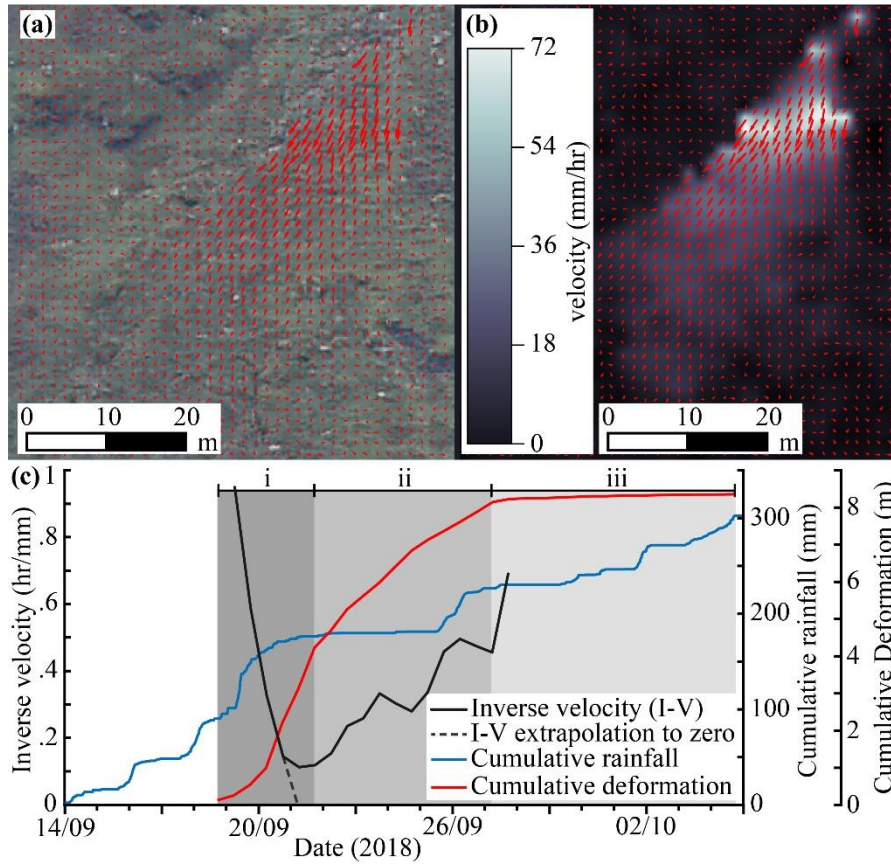
601  
602  
603  
604

**Figure 8.** Antecedent Precipitation Index (API) with 37 mm and 62 mm thresholds. Rainfall intensity (data loss 13 November to 05 December) with storms >10h duration exceeding the I-D threshold.

605

606

607

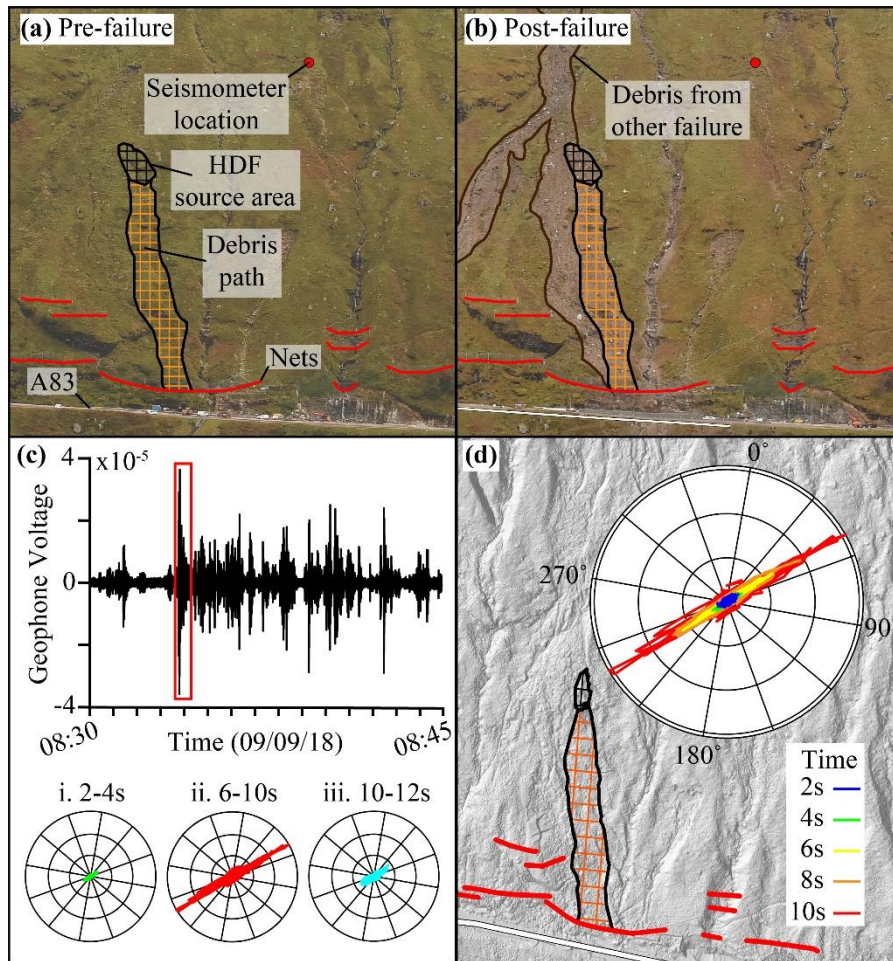


608

609

610

**Figure 9.** (a) PIVLab deformation vector plot (Thielicke and Stamhuis, 2014). (b) Velocity heat map. (c) Cumulative rainfall, cumulative deformation, and I-V.



611  
 612 **Figure 10.** (a) Pre-failure HDF source and seismometer location. (b) Post-failure. (c) Fifteen-  
 613 minute seismogram with HDF signal (red box) and three hodogram time-steps (i, ii, iii). (d)  
 614 Hillshade with HDF location and ten second stacked hodogram.

615  
 616  
 617  
 618  
 619  
 620  
 621  
 622  
 623  
 624

625 **Table 1.** Summary of contribution (by area and volume) of different material source areas to  
 626 the slope failure types occurring at the site

627  
 628

	<b>Debris Cones</b>	<b>Till</b>	<b>Regolith</b>
Number of debris flows and debris falls	11	21	11
Number of creep landslides	7	3	0
% areal slope coverage	22	61	18
% source area volume contribution	18	67	15

629  
 630

**Table 2.** Descriptive statistics for the depth profiles in Figure 4.

	<b>Inventory landslide number</b>					
	<b>41</b>	<b>47</b>	<b>48</b>	<b>49</b>	<b>50</b>	<b>51</b>
<b>Material</b>	Debris	Debris	Till	Debris	Regolith	Debris
<b>Minimum depth</b>	0.03	0.63	0.21	0.47	0.13	0.34
<b>Maximum depth</b>	2.3	7.6	1.61	1.79	1.75	3.27
<b>Average depth</b>	0.79	3.33	0.94	0.85	0.83	1.54
<b>Standard deviation of profile depth</b>	0.62	1.82	0.43	0.32	0.34	0.7

631 **Table 2 (Cont.).** Descriptive statistics for the depth profiles in Figure 4.

	<b>Inventory landslide number</b>					
	<b>53</b>	<b>55</b>	<b>57</b>	<b>58</b>	<b>64</b>	<b>65</b>
<b>Material</b>	Regolith	Regolith	Till	Till	Till	Till
<b>Minimum depth</b>	0.08	0.32	0.53	0.2	0.27	0.04
<b>Maximum depth</b>	1.27	1.22	0.72	1.93	2.6	3.2
<b>Average depth</b>	0.64	0.81	0.4	1.02	1.54	2.15
<b>Standard deviation of profile depth</b>	0.04	0.24	0.74	0.49	0.61	0.79

632

**Table 3.** Warning light and on-slope alert operation confusion matrix.

<i>% of study period</i>	<b>Landslide</b>	<b>No Landslide</b>
<b>Warning lights ON / On-Slope ON</b>	<b>6.6%</b> 7.7%	<b>4.1%</b> 11.1%
<b>Warning lights OFF / On-Slope OFF</b>	<b>2.8%</b> 1.1%	<b>86.5%</b> 80.1%

633

634

**Table 4.** API and I-D threshold confusion matrix. Current LMP statistics are summarised in Table 3.

635

<i>% of study period</i>	Landslide	No Landslide
<b>API &gt; threshold / I-D &gt; threshold</b>	<b>29.5%</b> 8.2%	<b>0.8%</b> 5.7%
<b>API &lt; threshold / I-D &lt; threshold</b>	<b>3.3%</b> 0.0%	<b>81.0%</b> 86.1%

636